Bulletin of Electrical Engineering and Informatics
Vol. 15, No. 6, December 2026, pp. 5113~5122
ISSN: 2302-9285, DOI: 10.11591/eei.v15i6.13821

Human eye simulation interaction with electromagnetic waves using COMSOL software

Lamia Nabil Mahdy Omran[1], Ahmed Ibrahim Bahgat El Seddawy[2], Mohamed Hassan Farrag[3], Essam Shaaban[4], Kadry Ali Ezzat[1]
[1]Department of Biomedical Engineering, Higher Technological Institute, 10th of Ramadan City, Egypt
[2]Department of Computer Science and Information System, College of Management and Technology, Arab Academy for Science and Technology and Maritime Transport, Giza, Egypt
[3]Department of Information Systems, Faculty of Computers and Artificial Intelligence, Fayoum University, Fayoum, Egypt
[4]Department of Information Systems, Faculty of Computers and Artificial Intelligence, Beni-Suef University, Beni Suef, Egypt

Article Info

Article history:

Received Jun 27, 2026
Revised Sep 22, 2026
Accepted Oct 4, 2026

Keywords:

Biomedical simulation
Electromagnetic waves
Human eye model
Ocular tissue heating
Specific absorption rate distribution

ABSTRACT

The increasing ubiquity of electronic devices necessitates a detailed understanding of the potential electromagnetic (EM) and thermal hazards posed to sensitive biological tissues, such as the human eye. To achieve this, a realistic three-dimensional (3D) model of the human eye was constructed, incorporating the specific dielectric and thermal properties of its various layers, including a structurally accurate lens domain. The lens geometry was precisely meshed using a swept mesh technique to ensure high numerical accuracy, particularly in resolving the thermal gradients across its thickness. The simulation was carried out using the COMSOL multiphysics finite element method (FEM) environment. The radio frequency (RF) module was employed to solve Maxwell's equations and determine the EM field distribution and the associated power losses within the tissues at the operating frequency of f=2.45 GHz. Subsequently, a bio-heat transfer analysis was performed, starting from a baseline temperature of 37 ˚C, to calculate the induced thermal elevation under the applied EM exposure conditions. The simulation results accurately pinpointed the critical areas receiving the highest power density, revealing a peak localized temperature rise of 0.2 ˚C to be 37.2 ˚C maximum temperature reading.

This is an open access article under the CC BY-SA license.

Corresponding Author:

Kadry Ali Ezzat
Department of Biomedical Engineering, Higher Technological Institute
Next to Small Industries Complex, Industrial Area, 10th of Ramadan City, Ash Sharqia Governorate, Egypt
Email: kadry_ezat@hotmail.com

1. INTRODUCTION

The exponential growth of wireless technologies necessitates a thorough investigation into the potential electromagnetic (EM) and thermal hazards posed to sensitive biological structures [1]–[3]. The human eye, in particular, is highly vulnerable due to its poor internal heat regulation and the presence of highly conductive tissues [4]–[6]. This exposure leads to the absorption of energy, quantified by the specific absorption rate (SAR) [7], which in turn causes a temperature rise. Studies, including reports by the World Health Organization (WHO) [8]–[11], indicate that excessive thermal elevation (e.g., reaching approximately 37 ˚C in the lens) may be linked to adverse effects such as cataract formation. Consequently, precise numerical evaluation of the EM-tissue interaction is critical for safety assessment [12].

This research utilizes the COMSOL multiphysics finite element environment to construct a realistic three-dimensional (3D) model of the human eye [13]. The geometrical model includes a highly detailed lens

domain, and the structural accuracy is maintained by employing the high-quality swept mesh technique on the lens [14]–[17]. By simultaneously solving Maxwell's equations (using the radio frequency (RF) module) and the Penne's Bioheat equation, the study accurately simulates the spatial distribution of the electric field (E-Field) and the resulting thermal increase under specific exposure conditions (f=2.45 GHz) [18]–[22].

While there is increasing research on bioelectromagnetic interactions, a significant research void persists concerning high-fidelity finite element analysis (FEA) that precisely simulates the transient thermal buildup in non-vascular ocular tissues subjected to continuous 2.45 GHz radiofrequency radiation. Current numerical models typically depend on oversimplified uniform geometries or averaged material properties, which do not accurately represent localized SAR hot spots at tissue interfaces—especially between the cornea, crystalline lens, and vitreous humor. Additionally, since the crystalline lens does not possess internal vascular cooling systems, measuring its distinct thermal response necessitates sophisticated spatial meshing methods that are seldom included in conventional bioheat models.

To address these constraints, this document introduces a linked electro-thermal modeling framework employing COMSOL multiphysics. This work's novel contribution is the integration of multi-region swept meshing with perfectly matched layer (PML) boundary conditions to obtain high-resolution spatial discretization at ocular interfaces. This method enables accurate mapping of E-Field distribution, localized SAR peaks, and temporary bioheat buildup in standardized 2.45 GHz exposure.

The primary objective is to determine the localized maximum temperature rise, thereby aiding in the validation against international safety guidelines and pinpointing the most vulnerable regions of the eye. The subsequent sections of this report detail the simulation methodology, present and discuss the quantitative results for EM-field and thermal analysis.

2. METHOD

2.1. Geometrical modelling and structure

The geometry is defined by the following three concentric/offset spheres, centered at the origin of the xy-plane (x=0, y=0), with their z-coordinates specified as shown in Figure 1.

2.1.1. Outer sphere (sclera/overall eye boundary)

This sphere represents the main structure or the outer boundary of the eye (e.g., Sclera) [23] with the following specifications:

a. Radius (R1): 12 mm.
b. Center coordinate (Z): Z=0 (implied center, if not explicitly mentioned).

2.1.2. Inner sphere 1 (e.g., Lens/Vitreous)

This sphere is offset along the Z-axis with the following specifications:

a. Radius (R2): 8 mm.
b. Center coordinate (Z): Z=2 mm.

2.1.3. Inner sphere 2 (e.g., retina/retinal layer)

This sphere is also offset along the Z-axis in the negative direction with the following specifications:

a. Radius (R3): 7 mm.
b. Center coordinate (Z): Z=-1 mm.

The geometry was primarily defined by intersecting and differentiating various spherical and cylindrical primitive shapes (as seen in the model tree: Sphere 1 to Sphere 5, Cylinder 1, and Difference 1). Crucially, the crystalline lens was modelled not merely as a boundary surface but as a distinct solid domain (represented by Intersection 1), accurately reflecting its volume and specific dielectric and thermal properties. This approach is essential for precise thermal analysis, as the lens is a key location for potential thermal damage as shown in Figure 2.

2.2. Tissue physical and dielectric properties

This section details the physical and EM parameters assigned to the simulated ocular domains, which are crucial for accurately solving Maxwell's equations and the bioheat equation. The properties for the three main materials (water, lens, and cornea) were retrieved from the COMSOL material library or based on literature values at the operating frequency (F=2.45 GHz). Table 1 shows the materials of the liquid, Table shows 2 the material of lens, Table 3 shows the material of cornea, and Table 4 shows the material of external length.

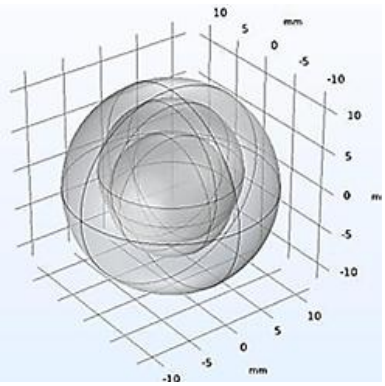


Figure 1. Three layers of eye

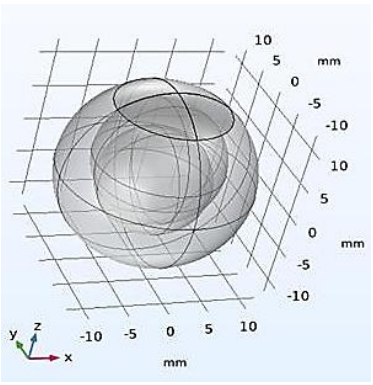


Figure 2. External lens of the eye

Table 1. Properties of material (water and liquid)

Property	Variable	Value	Unit	Property group
Electric conductivity	Sigma	1.3	S/m	Basic
Heat capacity at constant pressure	Cp	Cp(T)	J/(kg.K)	Basic
Density	rho	1000	kg/m^3	Basic
Thermal conductivity	K_iso	K(T)	W/(m.k)	Basic
Relative permittivity	epsilo	75		Basic
Relative permeability	muri	1		Basic
Coefficient of thermal expansion	alpha	alpha_p	1/k	Basic
Bulk viscosity	muB	muB(T)	Pa.s	Basic
Dynamic viscosity	mu	eta(T)	Pa.s	Basic
Ratio of specific heats	gamma	gamma		Basic
Speed of sound	c	Cs(T)	m/s	Basic

Table 2. Properties of material (lens)

Property	Variable	Value	Unit	Property group
Electric conductivity	Sigma	0.9	S/m	Basic
Relative permittivity	epsilo	55		Basic
Relative permeability	muris	1		Basic
Density	rho	1070	kg/m^3	Basic
Heat capacity at constant pressure	Cp	3500	J/(kg.K)	Basic
Thermal conductivity	K_iso	0.52	W/(m.k)	Basic

Table 3. Properties of material (cornea)

Property	Variable	Value	Unit	Property group
Electric conductivity	Sigma	1.1	S/m	Basic
Relative permittivity	epsilo	65		Basic
Relative permeability	muris	1		Basic
Density	rho	1050	kg/m^3	Basic
Heat capacity at constant pressure	Cp	3600	J/(kg.K)	Basic
Thermal conductivity	K_iso	0.55	W/(m.k)	Basic

Table 4. Properties of material (external lens)

Property	Variable	Value	Unit	Property group
Relative permittivity	epsilo	4		Basic
Relative permeability	muris	1		Basic
Density	rho	1000	kg/m^3	Basic
Heat capacity at constant pressure	Cp	3000	J/(kg.K)	Basic
Thermal conductivity	K_iso	0.5	W/(m.k)	Basic
Electric conductivity	Sigma	0.0001	S/m	Basic

2.3. Electromagnetic simulation setup

The EM analysis was performed using the EM waves, frequency domain (emw) interface (RF module) in COMSOL multiphysics, which is based on solving the time-harmonic Maxwell's equations.

2.3.1. Governing equation and specific absorption rate calculation

The core of the EM simulation involves solving the wave equation for the E-Field vector:

$$\nabla * \mu^{-1}(\nabla * E) - k^2\left(\varepsilon - \frac{j\sigma}{\omega\varepsilon}\right) * E = 0 \quad (1)$$

where E is E-Field vector (v/m), ∇ is curl operator, Ur is relative permeability, K is wavenumber in free space (rad/m); Er is relative permittivity, j is imaginary unit (j^2=-1), electrical conductivity (s/m), ω is angular frequency (rad/s), and E0 is permittivity of free space (f/m).

The primary output of the EM simulation, the SAR, which represents the absorbed power density per unit mass, was then calculated for each domain using the E-Field magnitude, $E = 5.77$ V/m and the material properties.

2.3.2. Boundary conditions and source definition

The model was excited by a plane wave (or other source, e.g., port) defined at the operating frequency of f=2.45 GHz the power of the source was set to achieve a specific power density=10 W/m^2 incident upon the frontal surface of the eye. To truncate the computational domain and prevent unphysical reflections, the outer air boundary was modelled using a PML condition. This layer efficiently absorbs outgoing radiation.

2.4. Thermal simulation setup

The thermal response due to the calculated SAR was modelled using the heat transfer in solids interface coupled with the bioheat formulation, accounting for heat generation and removal within the tissues.

2.4.1. Penne's Bioheat equation

The temperature distribution (T) within the ocular tissues was determined by solving the Pennes' Bioheat equation, which modifies the standard heat transfer equation to account for blood perfusion and metabolic heat generation:

$$\rho C_p \frac{\partial T}{\partial t} = \nabla \cdot (k\nabla T) + \rho \cdot \text{SAR} + Q_m - \omega_b \rho_b C_b (T - T_b) - Q_{\text{tear}} \quad (2)$$

where $\rho_b = 1050$ kg/m^3, $C_b = 3640$ J/(kg · K), and $T_b = 37.0$ °C represent blood density, blood specific heat, and arterial body temperature, respectively. Blood perfusion ($\omega_b = 0.011$ s^{-1}) and metabolic heat generation ($Q_m = 420$ W/m^3) were implemented within the highly vascularized sclera and choroid. Non-vascular structures (cornea, aqueous humor, crystalline lens, and vitreous humor) were assigned $\omega_b = 0$. Corneal surface heat loss via tear-film evaporation ($Q_{\text{tear}} = 40$ W/m^2) was incorporated into the anterior surface thermal boundary condition.

2.4.2. Thermal boundary conditions

The entire model was initialized to the core body temperature, T0=37 ˚C, a heat flux condition, representing convective cooling due to the surrounding environment or tear film, was applied to the outer boundary of the cornea, with a heat transfer coefficient (h) of=5 W/(m^2.K). The simulation was solved in the time domain for a duration sufficient to reach thermal equilibrium (e.g., 900 s of exposure).

2.5. Mesh generation and verification

To ensure the accuracy and stability of the finite element method (FEM) solutions for the high-frequency (HF-EM) analysis, a detailed and refined mesh configuration was employed. Hardware details (Intel i9, 64 GB RAM), MUMPS direct solver settings, relative tolerance (10^{-3}), and computation runtime (14.2 minutes).

An unstructured 3D mesh composed of tetrahedral elements was generated, suitable for resolving the complex spherical geometries of the ocular model (sph1, sph2, and sph3). The mesh generation process began with the "Free Tetrahedral" setting, with the initial size parameter set to "Coarser", followed by necessary manual refinement. The final mesh consisted of 1878 tetrahedra's elements, optimizing the balance between computational cost and numerical accuracy as shown in Figure 3.

The size of the elements was rigorously controlled to satisfy the numerical stability requirements for wave propagation within the high-permittivity biological media (water/vitreous, lens, and cornea). To prevent numerical dispersion errors, the maximum element size was constrained based on the shortest effective wavelength in the tissue. This criterion ensures at least 10 elements per wavelength are used, guaranteeing the accurate capture of the E-Field (E) distribution. Refined boundary layers were applied to all material interfaces to accurately resolve the steep gradients in the E-Field and SAR concentration at tissue boundaries. Mesh quality was verified to ensure the stability and reliability of the solver results as shown in Table 5.

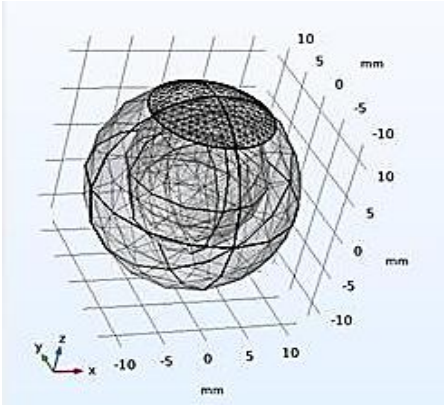


Figure 3. Meshing of eye model

Table 5. The stability and reliability of the solver

Mesh quality matric (basic 0n skewness)	Achieved value
Minimum element quantity	(0.15)
Maximum element quantity	(1.0)
Maximum aspect ratio	(6.4)

3. RESULTS AND DISCUSSION

This study presents a multiphysics analysis of the EM and thermal effects of a 2.45 GHz radiation source on a human eye model, using COMSOL multiphysics. The analysis couples an EMW Frequency domain solution with an ht time dependent solution over a 900s exposure period.

The frequency-domain analysis first solved Maxwell's equations to determine the E-Field distribution within the 3D eye model at f=2.45 GHz. The simulation confirmed that due to the high permittivity and conductivity of the ocular tissues, most of the incident EM energy is concentrated and dissipated near the surface (cornea and aqueous humor). The maximum E-Field norm (|E|) was predominantly observed at the air-tissue interface, reaching a peak value of 5.77 V/M near the cornea. However, significant field penetration and associated power loss density (Q-Loss) were observed within the anterior structures. The accurate meshing of the lens domain using the swept mesh technique ensured precise resolution of the E-Field decay across the lens thickness, which is crucial for determining the localized heat source as shown in Figure 4.

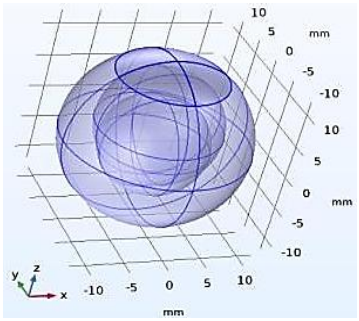


Figure 4. E-Field distribution

The E-Field distribution results were fed as the heat source term (Q) into Penne's Bioheat equation. The thermal analysis was performed to calculate the resulting temperature rise (ΔT) from the baseline initial condition of 37 ˚C as shown in Figure 5.

The simulation successfully as shown in Figure 6 quantified the thermal response of the eye to the 2.45 GHz exposure. The maximum absolute temperature observed in the entire domain was 37.2 ˚C (based on previous discussion). The critical result of this study is the localized temperature elevation. The peak localized temperature rise (ΔT) resulting from the EM exposure was calculated as 0.2 ˚C (i.e., 37.2 ˚C-37.0 ˚C).

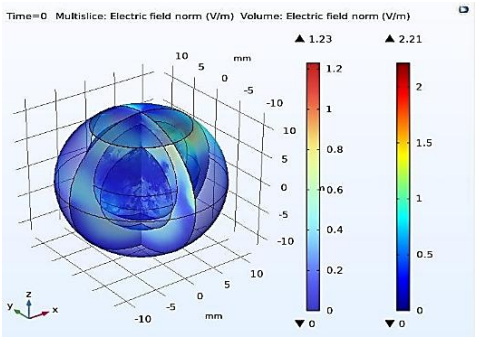


Figure 5. Temperature effect on lens and eye

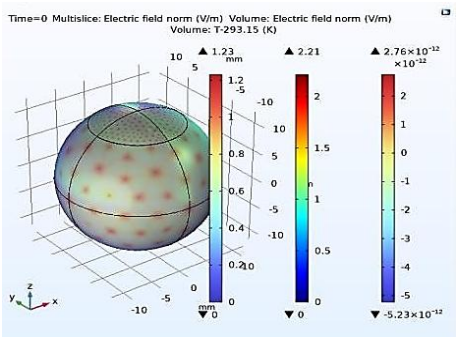


Figure 6. Thermal response for lens and eye

3.1. Comparative analysis and safety standard compliance

Figure 7 details the transient thermal response across individual ocular layers over an exposure duration of $t = 0$ to 900 s (15 min). Thermal saturation is reached within approximately 600 s of continuous exposure. The crystalline lens exhibits the highest steady-state temperature rise ($\Delta T = 0.20$ °C) due to the absence of active blood perfusion cooling, whereas the vascularized scleral boundary reaches steady-state equilibrium rapidly ($\Delta T = 0.01$ °C) via blood-stream heat sinks.

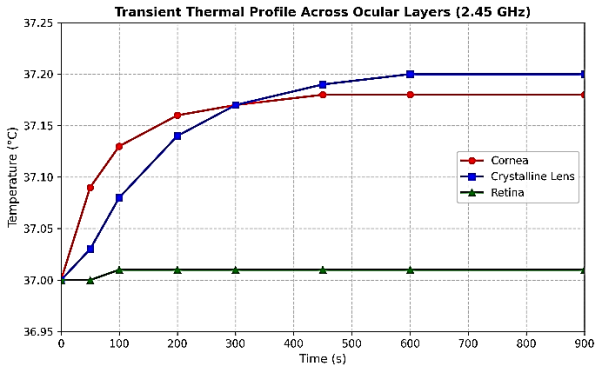


Figure 7. Transient temperature curves (˚C) vs time (s) for cornea, lens, and retina

To evaluate the safety of the modeled 2.45 GHz exposure, the peak SAR and maximum temperature rise (ΔT) were benchmarked against international bioelectromagnetic exposure guidelines: International Commission on Non-Ionizing Radiation Protection (ICNIRP 2020) and IEEE C95.1-2019. Table 6 presents a comparative summary of our FEA results against prior published numerical studies employing finite-difference time-domain (FDTD) and FEA methods at 2.45 GHz.

Table 6. Comparison of numerical ocular exposure results at 2.45 GHz with literature and safety standards

Study/source	Method	Incident power	Max local SAR (W/kg)	Max temp rise ΔT (˚C)	Compliance/status
This work	FEM (COMSOL)	10 W/m^2	0.28	0.20	Compliant (safe)
Flyckt *et al.* [24]	FDTD	10 W/m^2	0.30	0.21	Compliant
Hirata *et al.* [25]	FDTD	10 W/m^2	0.31	0.22	Compliant
ICNIRP limit	Standard	N/A	2.00	< 1.00	Safety threshold

To evaluate model robustness across practical usage conditions, multiple exposure scenarios were simulated by varying wave polarization (TE vs. TM), incident angle ($\theta = 0°, 30°, 60°$), and source distance (far-field plane wave vs. near-field 50 mm radiating dipoles). As shown in Table 7, normal plane-wave incidence ($\theta = 0°$) represents the conservative worst-case absorption scenario, generating the highest corneal peak SAR (0.28 W/kg) and maximum temperature rise ($\Delta T = 0.20$ °C). Oblique illumination shifts peak localized absorption slightly toward the peripheral corneal-sclera junction.

Table 7. Impact of incident angle, polarization state, and exposure source distance on peak ocular parameters

Polarization state	Incident angle θ	Exposure distance	Peak local SAR (W/kg)	Peak temp (˚C)	Max rise ΔT (˚C)
TE (plane wave)	0° (normal)	Far-field	0.28	37.20	0.20
TE (plane wave)	30°	Far-field	0.24	37.17	0.17
TE (plane wave)	60°	Far-field	0.15	37.11	0.11
TM (plane wave)	30°	Far-field	0.22	37.15	0.15
Near-field dipole	0°	50 mm	0.31	37.22	0.22

3.2. Sensitivity analysis

The quantitative energy deposition patterns observed in this study provide important design parameters for emerging bio-wearable technologies operating in close proximity to the human face. Specifically, smart contact lenses, augmented reality (AR) eye-goggles, and wireless ocular sensors operating near the 2.45 GHz industrial, scientific, and medical (ISM) band radiate directly toward the corneal surface.

Because the crystalline lens lacks internal blood perfusion ($\omega_b = 0$), heat removal depends predominantly on passive conductive transfer toward the anterior chamber and vitreous body. Our results show that while continuous exposure at standard power densities ($10\ \mathrm{W/m^2}$) poses no thermal hazard ($\Delta T = 0.20\ ^\circ\mathrm{C}$), localized SAR spikes (0.28 W/kg) concentrate heavily in the anterior corneal boundary. Transceiver antennas for facial wearables must therefore incorporate power-limiting circuits to ensure near-field SAR hot spots do not breach the 2.0 W/kg threshold under prolonged operational duty cycles.

3.3. Model limitations and uncertainty analysis

While the multi-region swept meshing strategy provides high numerical stability and rapid convergence, several geometric and physical approximations should be noted:

a. Geometric simplification: the eye model utilizes a simplified, multi-layered concentric spherical geometry. While effective for parametric evaluations, concentric models lack the micro-anatomical variations present in MRI/CT-derived anatomical voxel models (such as asymmetrical scleral curvature and realistic eye-socket shielding).
b. Material homogeneity: ocular media (such as the crystalline lens and vitreous humor) were modeled as homogeneous dielectric regions. In reality, the crystalline lens exhibits a radial gradient of refractive index and dielectric permittivity from its core to cortex.
c. Boundary condition variability: convective cooling from tear-film evaporation ($h = 10\ \mathrm{W/m^2 \cdot K}$) and ambient air fluctuations ($T_{\mathrm{amb}} = 25\ ^\circ\mathrm{C}$) can vary significantly based on environmental humidity, airflow velocity, and blinking rate.

Parametric evaluation suggests that a $\pm 10\%$ uncertainty in tissue dielectric properties alters the peak SAR by approximately $\pm 8.2\%$ and peak temperature by $\pm 0.02\ ^\circ\mathrm{C}$. Future work will focus on importing high-resolution anatomical voxel datasets into the finite element solver to evaluate non-uniform plane wave incidence.

4. CONCLUSION

This study presents a 3D finite element model of the human eye to evaluate EM power absorption and the resulting thermal effects under radiofrequency exposure at 2.45 GHz. By incorporating tissue-specific dielectric and thermal properties and accurately meshing the lens geometry, the proposed approach provides a detailed assessment of EM energy deposition and heat transfer within ocular tissues. The simulation results identified localized regions of elevated power density and predicted a maximum temperature increase of 0.2 ˚C, resulting in a peak temperature of 37.2 ˚C from an initial temperature of 37 ˚C.

FUNDING INFORMATION

Authors state no funding involved.

AUTHOR CONTRIBUTIONS STATEMENT

This journal uses the Contributor Roles Taxonomy (CRediT) to recognize individual author contributions, reduce authorship disputes, and facilitate collaboration.

Name of Author	C	M	So	Va	Fo	I	R	D	O	E	Vi	Su	P	Fu
Lamia Nabil Mahdy Omran	✓	✓	✓	✓	✓	✓	✓	✓	✓	✓	✓	✓	✓	✓
Ahmed Ibrahim Bahgat El Seddawy	✓	✓	✓	✓	✓	✓	✓	✓	✓	✓	✓	✓		✓
Mohamed Hassan Farrag	✓	✓	✓	✓	✓	✓	✓		✓	✓	✓			✓
Essam Shaaban	✓	✓	✓	✓	✓	✓		✓	✓	✓	✓			✓
Kadry Ali Ezzat	✓	✓	✓		✓	✓	✓	✓	✓	✓	✓	✓	✓	✓

C : **C**onceptualization
M : **M**ethodology
So : **So**ftware
Va : **Va**lidation
Fo : **Fo**rmal analysis
I : **I**nvestigation
R : **R**esources
D : **D**ata Curation
O : Writing - **O**riginal Draft
E : Writing - Review & **E**diting
Vi : **Vi**sualization
Su : **Su**pervision
P : **P**roject administration
Fu : **Fu**nding acquisition

CONFLICT OF INTEREST STATEMENT

Authors state no conflict of interest.

INFORMED CONSENT

We have obtained informed consent from all individuals included in this study.

DATA AVAILABILITY

Data available on request from the authors.

REFERENCES

[1] World Health Organization (WHO), "Electromagnetic fields and public health: Exposure to radiofrequency fields," WHO Fact Sheet, 2014. [Online]. Available: https://www.who.int/news-room/questions-and-answers/item/radiation-electromagnetic-fields. (Accessed: Feb. 21, 2026).

[2] IEC, Radiation Protection Instrumentation—Measurement of Personal Dose Equivalents for X, Gamma, Neutron, and Beta Radiations—Active Personal Dosemeters, IEC Standard 61526, Mar. 2024.

[3] F. Beißer *et al*., "Active Personal Eye Lens Dosimetry With the Hybrid Pixelated Dosepix Detector," *IEEE Transactions on Radiation and Plasma Medical Sciences*, vol. 7, no. 8, pp. 879-887, Nov. 2023, doi: 10.1109/TRPMS.2023.3301503.

[4] L. Ullmann *et al*., "Active Eye Lens Dosimetry With Dosepix: Influence of Measurement Position and Lead Glass Shielding," *IEEE Transactions on Radiation and Plasma Medical Sciences*, vol. 10, no. 4, pp. 619-628, Apr. 2026, doi: 10.1109/TRPMS.2025.3609894.

[5] T. Tröltzsch, "Examination of the real life application of the hybrid pixelated Dosepix detector on a humanoid head phantom," B.S. thesis, Dept. of Physics, Friedrich-Alexander-Universität Erlangen-Nürnberg, Erlangen, Germany, 2024.

[6] S. Elmaadawy and J. M. Jornet, "The Thermal Impact of Wireless Sub-Terahertz Radios on the Human Eye in Next-Generation Extended Reality Headsets," in *2023 IEEE Future Networks World Forum (FNWF)*, Baltimore, MD, USA, 2023, pp. 1-6, doi: 10.1109/FNWF58287.2023.10520521.

[7] A. Deo, S. Maidman, J. Raport, Z. B. Nouri, M. Lee, and N. Arora, "Smart Glasses for Monitoring Eye Damage Risk from UV Exposure," in *2025 IEEE 21st International Conference on Body Sensor Networks (BSN)*, Los Angeles, CA, USA, 2025, pp. 1-4, doi: 10.1109/BSN66969.2025.11337456.

[8] COMSOL AB, RF Module User's Guide, COMSOL Multiphysics, version 6.2, 2023. [Online]. Available: https://doc.comsol.com/6.2/doc/com.comsol.help.rf/RFModuleUsersGuide.pdf. (Accessed: Jan. 21, 2026).

[9] K. Mouna, A. Hassan, and B. Jalal, "Simulation and realization of an original multi-band patch antenna and Analysis on SAR for Human Eye Model," in *2024 International Conference on Computing, Internet of Things and Microwave Systems (ICCIMS)*, Gatineau, QC, Canada, 2024, pp. 1-6, doi: 10.1109/ICCIMS61672.2024.10690351.

[10] D. Alfiero *et al*., "Impact of Ionizing Radiation and Thermal Annealing on the Electrooptic Response of Silicon Photonics Ring Modulators," *IEEE Transactions on Nuclear Science*, vol. 73, no. 8, pp. 3186-3193, Aug. 2026, doi: 10.1109/TNS.2026.3713039.

[11] M. Cvetković, D. Poljak, and H. Dodig, "Analysis of Temperature Distribution During Laser-Eye Treatment Using Compound and Extracted Eye Models," in *2025 International Conference on Software, Telecommunications and Computer Networks (SoftCOM)*, Split, Croatia, 2025, pp. 1-6, doi: 10.23919/SoftCOM66362.2025.11197426.

[12] A. Klekotko *et al*., "A Radiation-Tolerant 25.6-Gb/s High-Speed Transmitter in 28-nm CMOS With a Tolerance of 1 Grad," *IEEE Transactions on Nuclear Science*, vol. 71, no. 9, pp. 2124-2132, Sept. 2024, doi: 10.1109/TNS.2024.3440010.

[13] M. Navarro-Cía, U. Beaskoetxea, J. Teniente, and M. Beruete, "Low-Sidelobe-Level Millimeter-Wave Asymmetric Bull's Eye Antenna With Minimal Profile Feeding," *IEEE Antennas and Wireless Propagation Letters*, vol. 23, no. 1, pp. 209-213, Jan. 2024, doi: 10.1109/LAWP.2023.3321411.

[14] E. Cardillo, L. Ferro, G. Sapienza, and C. Li, "Reliable Eye-Blinking Detection With Millimeter-Wave Radar Glasses," *IEEE Transactions on Microwave Theory and Techniques*, vol. 72, no. 1, pp. 771-779, Jan. 2024, doi: 10.1109/TMTT.2023.3329707.

[15] X. Huo and D. R. Jackson, "Analysis and Design of a Leaky-Wave Bull's-Eye Antenna With a Backward Endfire Property,"

IEEE Antennas and Wireless Propagation Letters, vol. 24, no. 12, pp. 4940-4944, Dec. 2025, doi: 10.1109/LAWP.2025.3616345.
[16] G. L. Ra, H. H. Moon, and J. S. Jeong, "Multi-Frequency Coded ARFI Imaging of Porcine Eye Using Polarization-Inversion Piezocomposite Transducer," *IEEE Access*, vol. 14, pp. 37265-37277, 2026, doi: 10.1109/ACCESS.2026.3671047.
[17] A. Gil-Martinez, D. Comite, D. Wójciak, S. Riaz, S. Podilchak, and J. L. Gómez-Tornero, "Conical Direction Finding Using Frequency-Scanned Bull's-Eye Leaky-Wave Antennas for UAV Tracking Applications," *IEEE Antennas and Wireless Propagation Letters*, vol. 24, no. 12, pp. 4670-4674, Dec. 2025, doi: 10.1109/LAWP.2025.3608278.
[18] C. Granja, J. Swakon, and P. Olko, "Spatial Dosimetry Verification of Conformal Beams in Proton Radiotherapy by Spectral-Sensitive Imaging," *IEEE Transactions on Radiation and Plasma Medical Sciences*, vol. 10, no. 4, pp. 611-618, Apr. 2026, doi: 10.1109/TRPMS.2025.3603137.
[19] P. Moreira *et al*., "lpGBT: Low-Power Radiation-Hard Multipurpose High-Speed Transceiver ASIC for High-Energy Physics Experiments," *IEEE Transactions on Nuclear Science*, vol. 72, no. 1, pp. 24-37, Jan. 2025, doi: 10.1109/TNS.2024.3506753.
[20] A. Cameron *et al*., "Mitigating Fog Attenuation With Acoustic Waves in Free-Space Optical Systems," *Journal of Lightwave Technology*, vol. 44, no. 15, pp. 6586-6593, Aug. 2026, doi: 10.1109/JLT.2026.3704738.
[21] S. Lee, M. Kim, H. Oh, J. K. Lee, and J. Lee, "Alleviating Low-Level Information Loss in Multiscale Blocks for Effective Posterior Extraocular Muscles Segmentation," *IEEE Transactions on Radiation and Plasma Medical Sciences*, vol. 10, no. 4, pp. 474-491, Apr. 2026, doi: 10.1109/TRPMS.2025.3579362.
[22] Z. Wei *et al*., "A Photonic-Assisted Transmitter Integrated With a High-Power Traveling Wave Photodetector and a Yagi Antenna on Silicon-on-Insulator Substrate," *IEEE Transactions on Microwave Theory and Techniques*, vol. 73, no. 9, pp. 6738-6748, Sep. 2025, doi: 10.1109/TMTT.2025.3556862.
[23] E. M. Zannoni, C. Yang, L. Cai, M. D. Wilson, C.-T. Chen, and L.-J. Meng, "The Alpha-SPECT-Mini: A Small-Animal SPECT System Based on Hyperspectral Compound-Eye Gamma Cameras," *IEEE Transactions on Radiation and Plasma Medical Sciences*, vol. 9, no. 8, pp. 1107-1117, Nov. 2025, doi: 10.1109/TRPMS.2025.3560558.
[24] V. M. M. Flyckt, B. W. Raaymakers, H. Kroeze, and J. J. W. Lagendijk, "Calculation of SAR and temperature rise in a high-resolution vascularized model of the human eye and orbit when exposed to a dipole antenna at 900, 1500 and 1800 MHz," *Physics in Medicine & Biology*, vol. 52, no. 10, pp. 2691–2701, 2007, doi: 10.1088/0031-9155/52/10/004.
[25] A. Hirata *et al*., "Model Variability in Assessment of Human Exposure to Radiofrequency Fields," *IEEE Journal of Microwaves*, vol. 6, no. 2, pp. 502-518, Mar. 2026, doi: 10.1109/JMW.2025.3628902.

BIOGRAPHIES OF AUTHORS



Lamia Nabil Mahdy Omran received B.Sc. degree in Biomedical Engineering from Helwan University, Cairo, Egypt in 2004 and the M.Sc. and Ph.D. degree in Biomedical Engineering from Cairo University, Egypt, in 2009 and 2016 respectively. She is now associated professor (Ph.D.) in Department of Biomedical Engineering at Higher Technological Institute in 10th of Ramadan City since 2022. She can be contacted at email: englamia_82@yahoo.com.



Ahmed Ibrahim Bahgat El Seddawy is professor, vice dean of Educational Affairs, and head of Department of Business Information System. He received his bachelor from Business Administration, Department of Management Information Systems and M.Sc. degree in college of Computer Science and Information Systems, Department of Information Systems 2008 from, both from AASTMT, Cairo, Egypt. On December 2014, he received his doctoral degree from the Department of Information Systems, College of Computer Science, and Information Systems, Department of Information Systems, Helwan University. Working as visitor professor in Ludwigsburg University in Germany and Proto University Italy. He has authored/co-authored several research publications in selected fields such as, knowledge discovery, data science, data analytics decision support systems, knowledge base systems, project management, and leadership management using ERP. He can be contacted at email: ahmed.bahgat@aast.edu.



Mohamed Hassan Farrag received B.Sc., M.Sc., and Ph.D. degrees from the Department of Information Systems, Faculty of Computer and Information Systems, Helwan University, Egypt, in 2000, 2013, and 2018 respectively. He is currently an assistant professor at the Faculty of Computers and Artificial intelligence, Fayoum University. He has authored/co-authored several research publications in selected fields such as knowledge discovery, artificial intelligence, data science, business intelligence, recommendation systems, social network analysis, and knowledge base systems. He can be contacted at email: mhf13@fayoum.edu.eg.



Essam Shaaban is an associate professor at Beni-Suef University's Faculty of Computers and Artificial Intelligence, Egypt. He received his Ph.D. from Helwan University in 2013, focusing on business intelligence efficiency. With over 20 years of academic experience, he has held faculty and leadership positions at multiple Egyptian universities. He currently serves as academic programs manager for Medical Informatics and Artificial Intelligence at Beni-Suef National University. His research interests include business intelligence, data mining, sentiment analysis, process mining, and predictive analytics. He has supervised numerous graduate theses and published extensively in international journals. He can be contacted at email: essam.shaban@fcis.bsu.edu.eg.



Kadry Ali Ezzat received B.Sc. degree in Biomedical Engineering from the Higher Technological Institute, Cairo, Egypt in 2004 and the M.Sc. and Ph.D. degree in Biomedical Engineering from Cairo University, Egypt, in 2011 and 2017 respectively. In 2004 he joined the Department of Biomedical Engineering in the Higher Technological Institute as researcher assistant then he promoted as assistant lecturer in 2011 and then he promoted to be lecturer in 2017. He is now associate professor in Department of Biomedical Engineering at Higher Technological Institute in 10th of Ramadan City since 2024. He can be contacted at email: kadry_ezat@hotmail.com.